AGU ADVANCING EARTH AND SPACE SCIENCES

Geophysical Research Letters

RESEARCH LETTER
10.1029/2024GL110506

GOLD Observations of the Thermospheric Response to the 10–12 May 2024 Gannon Superstorm

J. S. Evans[1], J. Correira[1], J. D. Lumpe[2], R. W. Eastes[3], Q. Gan[3], F. I. Laskar[3], S. Aryal[3], W. Wang[4], A. G. Burns[4], S. Beland[3], X. Cai[3], M. Codrescu[5], S. England[6], K. Greer[3], A. Krywonos[7], W. E. McClintock[3], T. Plummer[3], and V. Veibell[1]

[1]Computational Physics, Inc., Springfield, VA, USA, [2]Computational Physics, Inc., Boulder, CO, USA, [3]Laboratory for Atmospheric and Space Physics, University of Colorado, Boulder, CO, USA, [4]HAO, NCAR, Boulder, CO, USA, [5]Space Weather Prediction Center, NOAA, Boulder, CO, USA, [6]Virginia Tech, Blacksburg, VA, USA, [7]Florida Space Institute, University of Central Florida, Orlando, FL, USA

Key Points:

- GOLD disk images of $\Sigma O/N_2$ and neutral temperature link storm time dynamics with changes in thermospheric composition and temperature
- We observe a previously unseen spatial morphology in $\Sigma O/N_2$, neutral temperature, and total electron content
- Peak equator-to-pole temperature differences exceed 400 K but relax to pre-storm conditions well before $\Sigma O/N_2$

Supporting Information:

Supporting Information may be found in the online version of this article.

Correspondence to:

J. S. Evans,
evans@cpi.com

Citation:

Evans, J. S., Correira, J., Lumpe, J. D., Eastes, R. W., Gan, Q., Laskar, F. I., et al. (2024). GOLD observations of the thermospheric response to the 10–12 May 2024 Gannon superstorm. *Geophysical Research Letters*, *51*, e2024GL110506. https://doi.org/10.1029/2024GL110506

Received 6 JUN 2024
Accepted 25 JUL 2024

Abstract After days of intense solar activity, active region AR3664 launched seven CMEs toward Earth producing an extreme G5 geomagnetic storm commencing at 17:05 UT on 10 May 2024. The storm impacted power grids, disrupted precision navigational systems used by farming equipment, and generated aurora seen around the globe. The storm produced remarkable effects on composition, temperature, and dynamics in the Earth's thermosphere that were observed by NASA's Global-scale Observations of the Limb and Disk (GOLD) mission and are reported here for the first time. We use synoptic disk images of $\Sigma O/N_2$ and neutral temperature (at ∼160 km) measured by GOLD to directly link dynamics resulting from the storm with dramatic changes in thermospheric composition and temperature. We observe a heretofore unseen spatial morphology simultaneously in $\Sigma O/N_2$, neutral temperature, and total electron content. Equator-to-pole temperature differences reach 400 K with high latitude peak neutral temperatures near 160 km exceeding 1400 K.

Plain Language Summary On Saturday 10 May 2024, the sun launched a wave of energized plasma toward the Earth. A large disturbance in the Earth's magnetic field associated with the solar wind resulted in an extreme geomagnetic storm. The storm impacted power grids, disrupted navigational systems used by farming equipment, and produced aurora seen around the globe. The storm produced remarkable effects in the Earth's upper atmosphere that were observed by NASA's Global-scale Observations of the Limb and Disk (GOLD) mission. In this letter, we use images measured by GOLD to directly link atmospheric dynamics resulting from the May 10–12 superstorm with dramatic changes in composition, temperature, and global circulation in the Earth's upper atmosphere. We observe previously unseen structure in the upper atmosphere associated with equator-to-pole temperature differences exceeding 400 K. Peak neutral temperatures near 160 km exceed 1400 K at high latitudes.

1. Introduction

Following days of intense solar activity, active region AR3664 hurled a series of seven CMEs (coronal mass ejections) toward Earth resulting in the commencement of an extreme G5 geomagnetic storm at 17:05 UT on Saturday 10 May 2024. The last G5 storm, which is well documented and widely known as the Halloween storm, occurred over 20 years prior in October 2003. The May 10–12 storm is now ranked among the top 20 Great Storms of the past 500 years (Hayakawa et al., 2024). The storm impacted power grids, disrupted navigational systems used by farming equipment in the Midwest and elsewhere (O'Callaghan & Billings, 2024), and produced aurora seen around the globe in both northern and southern hemispheres as far south as New Caledonia (magnetic latitude = −26.4°) and Puerto Rico (magnetic latitude = 27.2°) and as far north as the southern tips of South America and Africa. Not evident to the naked eye, however, were remarkable effects on composition, temperature, and dynamics in the Earth's thermosphere that were observed by NASA's Global-scale Observations of the Limb and Disk (GOLD) mission. While thermospheric effects from extreme geomagnetic storms have been well documented in the literature, there are no prior synoptic observations of dayside thermospheric effects on the scale and magnitude achieved by GOLD and reported here for the first time.

Neutral winds play an important role in the dynamics of the coupled Thermosphere-Ionosphere (TI) system. During geomagnetic storms, enhanced energy and momentum inputs in the high-latitude upper thermosphere lead to strong heating and ion drag, which affect global wind patterns and drive changes in both composition and

neutral temperature (Li et al., 2019). The resulting storm-time meridional winds are primarily equatorward with velocities reaching 500–800 m s^{-1} at high latitudes (Emery et al., 1999; Evans et al., 1979; Fuller-Rowell et al., 2002; Gardner & Schunk, 2010; Richmond & Lu, 2000). Dominant drivers of high-latitude meridional wind disturbances in the F-region are ion drag and pressure gradients (Li et al., 2019, and references therein). During the more intense geomagnetic storms, high-latitude meridional winds in the upper thermosphere propagate to lower latitudes. Temperature changes produced by vertical wind perturbations and a westward directed Coriolis force are the dominant storm-time processes that drive winds at middle and low latitudes (Buonsanto, 1999; Gan et al., 2024; Meriwether, 2008).

While the response of the thermosphere to geomagnetic activity has been well documented (Burns et al., 1995; Craven et al., 1994; Crowley, Emery, Roble, Carlson, & Knipp, 1989; Crowley, Emery, Roble, Carlson, Salah, et al., 1989; Crowley et al., 1995; Fuller-Rowell et al., 1996; Meier et al., 2005; Proelss, 1980, 1987; Strickland et al., 2001), simultaneous synoptic measurements of global scale changes in both composition and temperature, and how those changes evolve temporally and spatially, have not been available until now. Geographic maps of $\Sigma O/N_2$, the column density ratio of atomic oxygen to molecular nitrogen, from previous studies have shown significant depletions in atomic oxygen that extend from the polar regions to the equator during strong storms. $\Sigma O/N_2$ has been shown to be a key indicator of how thermospheric composition is perturbed at high latitudes and how the perturbed air is transported and evolves temporally as a result of dynamical forcing. Transported regions of depleted and enhanced $\Sigma O/N_2$ have also been shown to correlate well with changes in thermospheric temperatures (Meier et al., 2005). The objective of this letter is to use synoptic disk images of $\Sigma O/N_2$ and neutral temperature measured by GOLD to demonstrate the important link between changes in thermospheric composition and neutral temperature and the dynamics that ensued and evolved following the commencement of the May 10–12 event, which we propose to name the Gannon superstorm (see Acknowledgments).

2. Solar and Geomagnetic Conditions

Once ground- and space-based measurements detected a sequence of seven Earth-directed CMEs from the sun on May 8, NOAA's Space Weather Prediction Center (SWPC) issued a warning of a severe space weather event. After the first CME struck, the speed of the solar wind abruptly increased to over 700 km s^{-1}. South-pointing interplanetary magnetic fields emitted from the sun produced geomagnetic disturbances with a Dst index of nearly −400 (nT), whereas the ap60 magnetic index (Yamazaki et al., 2022) rapidly rose to 300 (nT), briefly spiked to over 400 (nT) early on May 11, and then gradually relaxed to pre-storm conditions between May 12 and 13, as seen in Figure 1. We note that Dst data shown in the figure are provisional. Therefore, it is likely that the final data will differ slightly. Solar activity as measured by the F10.7 cm index remained relatively stable before the onset of the storm until the storm ended around May 13, with peak variations <10%. A similar level of stability was observed in QEUV (integrated solar irradiance 1–45 nm; Strickland et al., 1995; J. Evans, Strickland, & Huffman, 1995; Correira et al., 2021) measured daily by GOLD at a two-hour cadence from 08:10 to 18:10 UT. Since the solar and geomagnetic indices indicate low activity on May 9 relative to the storm, we use this day as a pre-storm baseline when taking differences between storm and pre-storm data.

3. The GOLD Instrument

The GOLD instrument is a dual channel spectrograph observing Earth's ultraviolet emissions from 132 to 162 nm (Eastes et al., 2017; McClintock et al., 2020). The two channels, designated A and B, are in effect identical, independently commandable instruments, allowing for 2 different observing modes to be conducted simultaneously. Each channel consists of a rotating mirror mechanism that directs the incoming light onto a spherical telescope mirror, which then projects the light onto one of three possible slits. The combination of a concave toroidal mirror and concave toroidal grating is then used to disperse the input beam and image the entrance slit onto a microchannel plate (MCP) detector, forming a spectral-by-spatial image of the slit. Three slits can be used: high resolution (HR, 0.21 nm spectral resolution); low resolution (LR, 0.35 nm); and the occultation slit (OCC, 2.16 nm). The HR slit was used to collect all GOLD data shown in this letter. The GOLD mirror mechanism consists of two back-to-back tilted plane mirrors. The tilted orientation allows either the north or south hemisphere to be observed by flipping the mirror mechanism. Eastes et al. (2017) and McClintock et al. (2020) provide detailed information about the GOLD instrument, operations, and observing modes.

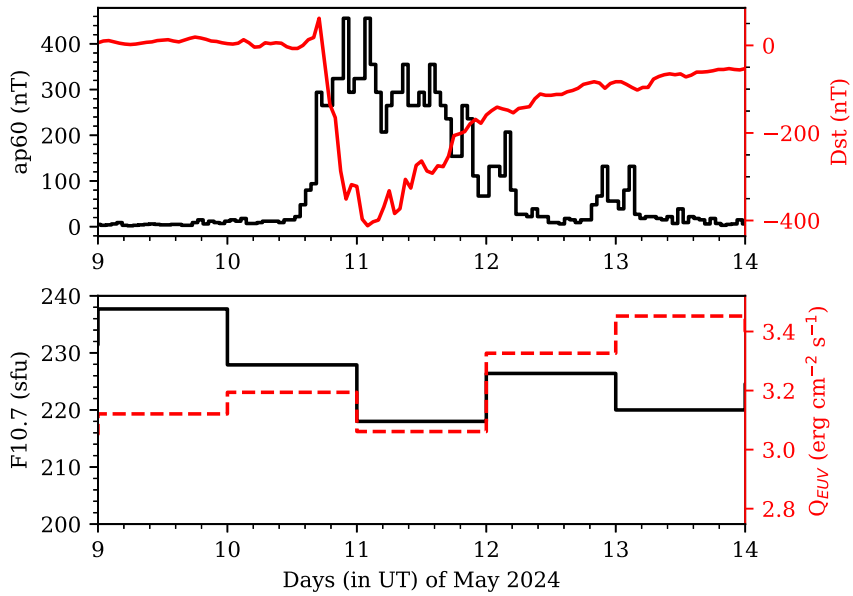

Figure 1. Top: Hourly ap60 version 3.0 geomagnetic index (black, left axis) and Dst (red, right axis) for 9–14 May 2024. Bottom: Daily solar F10.7 index (black, left axis) and daily averaged QEUV (integrated irradiance 1–45 nm; red, right axis) measured by GOLD for the same time frame as the top panel.

4. GOLD Observations

GOLD utilizes four nominal observation modes: day disk scans, limb scans, occultations, and night disk scans. These modes are referred to by their respective observation type codes: DAY, LIM, OCC, and NI1. Effective neutral atmospheric temperatures, contained in the Level 2 data product TDISK, are derived from DAY observations of molecular nitrogen (N_2) Lyman-Birge-Hopfield (LBH) band emissions ($a^1\ \Pi_g \rightarrow X^1\ \Sigma_g^+$). Details of the TDISK algorithm are described by Evans et al. (2024). The intensity ratio of 135.6 nm (135–137 nm) to LBH (140.5–148 nm) as observed by GOLD during disk scans is used to derive the column density ratio $\Sigma O/N_2$ contained in the GOLD Level 2 data product ON2. The $\Sigma O/N_2$ concept was introduced and discussed by Strickland et al. (1995) and Evans et al. (1995). A detailed description of the GOLD $\Sigma O/N_2$ algorithm is provided by Correira et al. (2021).

GOLD DAY observations, contained in Level 1C files (see links to the GOLD Release Notes and current data product versions provided in the Data Availability section), have a spatial resolution of approximately 125 km × 125 km at nadir. Spatial pixels at the Level 1C resolution contain a single spectrum. This letter uses TDISK Version 5 data, which utilizes four pixel spectral binning on a 2 × 2 spatially binned radiance spectra, with spatial binning performed first, followed by spectral binning. The spectra input to the Level 2 TDISK algorithm therefore have 250 km × 250 km spatial resolution and 0.64 nm spectral bin size. The spectral input to the Level 2 ON2 algorithm utilizes the native Level 1C spectral resolution with 2 × 2 spatial binning.

5. Discussion

To better understand the remarkable thermospheric storm-time response observed in GOLD data, we first summarize the conceptual picture of thermospheric storm-time dynamics proposed by Buonsanto (1999) and further elucidated by Meriwether (2008). Expansion of the polar neutral atmosphere is induced by particle and Joule heating at high latitudes. This expansion produces equatorward winds at high altitudes and upwelling followed by deviations from diffusive equilibrium due to an increase in the effective molecular mass and vertical advection by winds. The global thermospheric circulation is then altered by a high-to-low latitude pressure gradient generated by high latitude heating. Antisunward plasma convection within the polar cap also results in enhanced equatorward winds (Babcock & Evans, 1979; Fuller-Rowell et al., 1997; Straus & Schulz, 1976). These winds then transport thermal and composition disturbances to lower latitudes, resulting in higher temperatures and reduced $\Sigma O/N_2$ and $\Sigma O/O_2$ extending down to middle latitudes (Fuller-Rowell et al., 1997; Proelss, 1987).

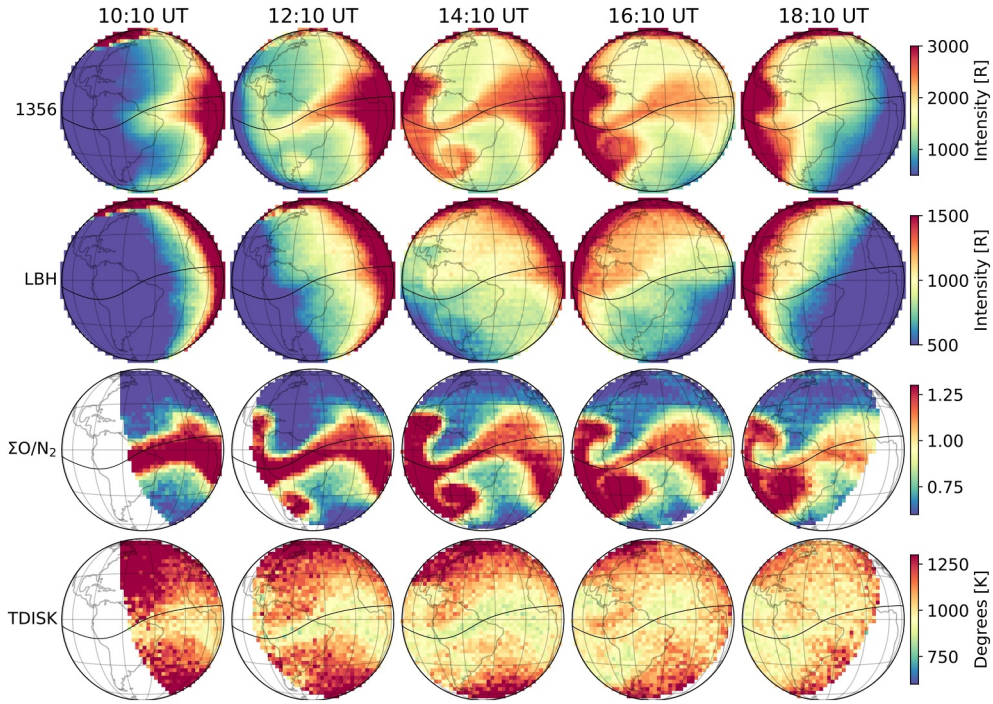

Figure 2. GOLD Level 2 data showing temporal and spatial evolution of the thermosphere during the storm on May 11. The first and second rows are the 1356 Å and LBH absolute radiances used as input to the $\Sigma O/N_2$ algorithm, while the last two rows show GOLD $\Sigma O/N_2$ and TDISK values. Full disk images shown are combined individual north and south hemisphere scans. Times listed at the top of each row are the time the north hemisphere scan started. A scan beginning at 08:10 UT with minimal dayside data is not shown. The black line indicates the geomagnetic equator.

Oxygen depleted air reaches the lowest latitudes on the nightside, and then rotates with the Earth into the morning sector. $\Sigma O/N_2$ enhancement also occurs at high latitudes, where downwelling occurs, just equatorward of the $\Sigma O/N_2$ depletion region. Both $\Sigma O/N_2$ enhancement and depletion air parcels are then transported toward lower latitudes (Burns et al., 1991, 1995; Fuller-Rowell et al., 1997; Rishbeth, 1989; Yu et al., 2021). Emmert et al. (2004) suggested that typically the largest equatorward disturbance winds, near 03:00 hr magnetic local time, are produced by high latitude pressure gradients induced by heating. As air moves equatorward, the flow rotates westward and the winds become more or less zonal, as the poleward Coriolis force is balanced by the equatorward pressure gradient force.

Figure 2 demonstrates the temporal and spatial evolution of the thermosphere over the course of May 11 as observed by GOLD. O I 135.6 nm and N_2 LBH radiances derived from GOLD spectra are shown in the first two rows, while derived GOLD Level 2 data products $\Sigma O/N_2$ and TDISK are shown in the third and fourth rows. Intensities shown are directly input into the $\Sigma O/N_2$ algorithm (along with solar zenith angle), while TDISK is derived by directly fitting the rotational structure of the LBH spectrum (137–148.5 nm) as described by Evans et al. (2024) (see Section 4). Disk images shown here are a composite of two consecutive DAY scans. Each scan covers a little more than half of the visible Earth as seen by GOLD. Dayside scan sequences begin with a northern hemisphere scan immediately followed by a southern hemisphere scan. For the purposes of creating these composite full disk images, the small region near the equator where the projection of the instrument slit overlaps from the two scans is averaged together. A DAY disk scan beginning at 08:10 UT is not shown as most of the Earth visible by GOLD is still in darkness and Level 2 values are not available.

The general global scale spatial morphology of the May 10–12 storm observed by GOLD exhibits several similarities to that seen in previous geomagnetic storms. Reduction of $\Sigma O/N_2$ occurs at higher latitudes due to heating and subsequent upwelling of air rich in molecular nitrogen. Regions of depleted $\Sigma O/N_2$ at higher latitudes are then transported to lower latitudes. Thermospheric heating due to particle and Joule heating at high latitudes is evident in the TDISK data. However, the morphology seen at mid latitudes and the equatorial region is stunning. This is, to the best of our knowledge, the first time such morphology has been observed in remotely sensed

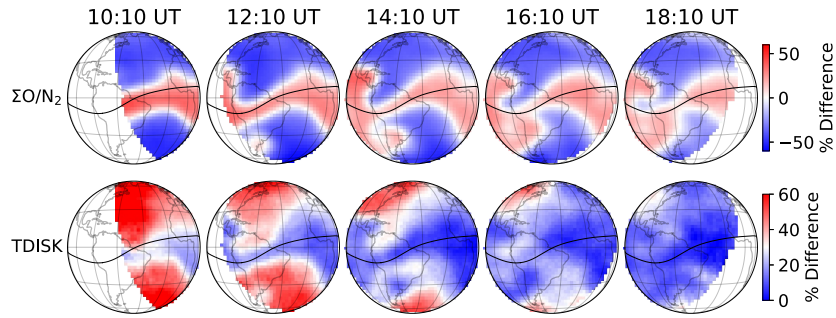

Figure 3. Time series of convolved $\Sigma O/N_2$ and TDISK data for May 11 shown as percent difference from the pre-storm baseline day of May 9. The data is convolved with a two dimensional Gaussian kernel in order to reduce noise in the TDISK data. As with Figure 2, a scan beginning at 08:10 UT with minimal dayside data is not shown.

thermospheric composition and temperature on the scale achieved by GOLD. The large scale structure in the thermosphere, which is attributable to longitudinal variations of meridional winds (driven by zonal winds and the Coriolis force) combined with a continuous push of meridional winds into the opposite hemisphere, can be seen north and south of the geomagnetic equator. While there is an appearance of a swirl or eddy in the structure, suggesting possible rotation, the two-hour cadence of GOLD observations during this event makes it difficult to diagnose how the structure evolved over time.

The evolution of $\Sigma O/N_2$ and TDISK as percent differences with respect to a pre-storm day is shown in Figure 3. May 9 (day of year 130) is used as the baseline for comparison in order to account for effects unrelated to the May 10–12 storm that may be present, as evident in Figure 2, particularly regarding variations in solar illumination. In order to reduce the noise seen in TDISK images (see bottom row of Figure 2), data shown in Figure 3 were smoothed by convolving the Level 2 data with a two–dimensional Gaussian kernel using the Astropy Gaussian2DKernel function (Astropy Collaboration et al., 2022). A standard deviation of 1.5 pixels (~3.5 pixels full width half maximum) was used for the Gaussian in both the *x* and *y* directions. An unsmoothed version of Figure 3 may be seen in Figure S1 in the Supporting Information S1. Smoothing was applied to $\Sigma O/N_2$ data as well.

The spatial morphology for both $\Sigma O/N_2$ and TDISK seen in Figure 2 is the same as in Figure 3, however the behavior of TDISK is much more clearly seen in the difference images. The difference images also make apparent the anti-correlation of $\Sigma O/N_2$ and TDISK, particularly at earlier times (see also Figure S2 in the Supporting Information S1). It is interesting to note that the spatial structure in the southern hemisphere slowly migrates toward the northwest, with the core of the structure appearing over the east coast of South America at 12:10 UT and moving off the west coast by the last scan at 18:10 UT. Furthermore, although $\Sigma O/N_2$ and TDISK are signatures of variability in the neutral atmosphere, both appear inclined to the geodetic equator and aligned with the geomagnetic equator. This is consistent with a similar alignment of TEC structure with the geomagnetic equator seen at 15:25 UT in Figure 4. Since F-region plasma motion is determined by E × B drifts perpendicular to the magnetic field as well as field-aligned wind transport and ambipolar diffusion, it is surprising that the structure in the southern hemisphere TEC data coincides spatially with the structure seen in both the $\Sigma O/N_2$ and temperature data shown in Figures 2 and 3.

At high latitudes, $\Sigma O/N_2$ is up to 50% lower during the storm compared to the pre-storm baseline, while TDISK is on the order of 50% higher. At equatorial latitudes, $\Sigma O/N_2$ shows a 50% increase over the baseline day, while TDISK shows little change with respect to the baseline day (note the difference in colors scales in Figure 3). Also of interest is the rapid relaxation of neutral temperatures as the storm subsides later in the day. Neutral temperatures return to near pre-storm baseline values over most of the observed globe by 18:10 UT while $\Sigma O/N_2$ continues to exhibit strong depletion features throughout the day on May 11. Strong latitudinal gradients and longitudinal dependence in the TDISK data at 14:10 UT relative to quiet periods on the days before and after May 11 are shown in Figure S3 in the Supporting Information S1.

Though nitric oxide (NO) is a minor species, it plays a significant role in determining the thermal structure of the thermosphere due to its strong infrared emission at 5.3 μm, which is an important cooling mechanism in the thermosphere (Mlynczak et al., 2003). Ionization of neutral atoms and molecules by precipitating electrons (1–10 keV) and protons (>10 keV) at high latitudes leads to the production of NO (Gérard & Barth, 1977; Burns

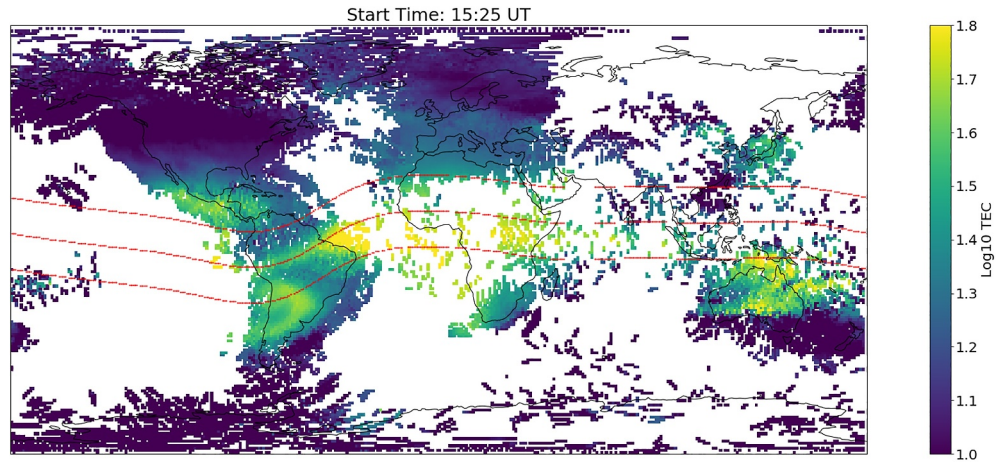

Figure 4. Mean total electron content (TEC; in log base 10 scale TECu) from 15:25–15:50 UT (25-min average) projected onto the geographic map. Notice the spatial morphology over South America that is also seen in $\Sigma O/N_2$ and TDISK (see Figures 2 and 3). The structure is seen forming around 11:00 UT and is visible until about 18:00 UT (see Movie S1). The magnetic equator (and ±15° magnetic latitudes) are shown in magenta for reference.

et al., 1989; C. A. Barth, 1992; Roble, 1992; Codrescu et al., 1997; Galand et al., 1999; C. Barth et al., 2003). Storm-time equatorward meridional winds transport both $\Sigma O/N_2$ depleted and NO enhanced air from high to low latitudes. $\Sigma O/N_2$ depleted air is observed to be anti-correlated with NO enhanced air on a global scale (Zhang et al., 2014). Different behaviors of $\Sigma O/N_2$ and NO on local scales are at least partially explained by the altitude dependence of the storm-time meridional winds, peak altitudes of $\Sigma O/N_2$ and NO variations, and the altitude dependent lifetime of NO. Thus, NO regulates the storm-time temperature enhancement, and can significantly affect temperature during the storm recovery phase. However, 3-D wind and temperature data are needed to quantify and characterize the effects of NO on temperature as observed in the GOLD data reported here.

It should be noted that the algorithm used for deriving $\Sigma O/N_2$ assumes that impact by photoelectrons is the only source of excitation for atomic oxygen and molecular nitrogen in the thermosphere. The presence of energetic electrons and protons in the auroral oval would be a source of contamination for the $\Sigma O/N_2$ algorithm. While this would result in an increased error in derived $\Sigma O/N_2$ values within the auroral oval, it does not impact the gross spatial morphology, nor does it apply to composition derived at subauroral latitudes. Regarding radiative recombination contamination affecting $\Sigma O/N_2$ data, Figure S4 in the Supporting Information S1 shows the O I 135.6 nm radiative recombination emission on the nightside at 08:10 UT for May 9 and 11. While the subauroral emission is clearly enhanced on May 11 relative to the baseline day, it is at the ∼15% level relative to the bright dayglow seen in Figure 2. Auroral contamination of TDISK is possible if incident auroral particles produce a deviation from the assumed N_2 vibrational populations (Aryal et al., 2022; Evans et al., 2024). However, even if such contamination is present, it is expected to produce a minor increase in uncertainty of the derived neutral temperatures (Budzien et al., 1994) and only within and poleward of the auroral oval.

6. Summary

The May 10–12 Gannon superstorm produced remarkable effects on composition, temperature, and dynamics in the Earth's thermosphere that were observed by NASA's GOLD mission and are reported here for the first time. In this letter, we have used GOLD disk images of $\Sigma O/N_2$ and neutral temperature (at ∼160 km) to directly link dynamics resulting from the storm with dramatic changes in thermospheric composition and temperature. We observe a previously unseen morphology in $\Sigma O/N_2$, neutral temperature, and TEC data simultaneously in universal time and spatial location that is attributable to longitudinal variations of meridional winds combined with a continuous push of meridional winds into the opposite hemisphere. However, due to a lack of concurrent wind observations, it is difficult to diagnose how and why the observed morphology was produced. A more detailed explanation of the causes of the observed spatial morphology will be the subject of a future paper.

We find peak neutral temperatures near 160 km exceeding 1400 K at high latitudes and equator-to-pole temperature differences that exceed 400 K (50%) relative to pre-storm conditions. These temperature differences are

largest in the early phases of the storm that are observable by GOLD on the dayside, but relax to pre-storm conditions more rapidly than $\Sigma O/N_2$, which exhibits significant depletion (50%) extending down to the geographic equator at least 12 hr after the first GOLD observation at 10:10 UT. Finally, we note that while $\Sigma O/N_2$, TDISK, and TEC appear aligned with the geomagnetic equator near the Americas, a southward asymmetry is apparent west of Africa on the eastern side of GOLD's field of view.

For over 5 years, the GOLD mission has significantly advanced our understanding of the thermospheric response to geomagnetic storms. GOLD provides unique synoptic scans from geosynchronous orbit for monitoring changes in thermospheric neutral composition and temperature associated with geomagnetic storms (Cai et al., 2020, 2023; Gan et al., 2020, 2024; Laskar et al., 2021, 2022). Having simultaneous observations of important state quantities (i.e., composition, temperature, and neutral winds) over a broad altitude range is crucial for fully understanding thermospheric energetics and dynamics during geomagnetically disturbed times.

An important but brief opportunity in this regard was enabled by leveraging the GOLD and Ionospheric Connection Explorer (ICON) missions. As noted in Gan et al. (2024), during a CME geomagnetic storm (3 and 4 November 2021), a 60%–70% depletion (enhancement) in GOLD $\Sigma O/N_2$ (TDISK) was observed, coincident with a ∼100 m/s deviation in ICON meridional winds. This provides observational evidence for the theoretical hypothesis that storm-driven temperature gradients at higher latitudes produce significant equatorward meridional circulation and push the $\Sigma O/N_2$ depletion bulge from higher to lower latitudes. The untimely demise of ICON and the stunning observations reported in this letter, however, highlight the necessity for global wind measurements and the importance of NASA's proposed Dynamical Neutral Atmosphere-Ionosphere Coupling (DYNAMIC) mission.

Data Availability Statement

GOLD Level 1C DAY and Level 2 ON2 and TDISK data used in this paper can be obtained at the GOLD website, https://gold.cs.ucf.edu/search/, and NASA's Space Physics Data Facility (SPDF), https://spdf.gsfc.nasa.gov/pub/data/gold/. GOLD data products are described in the GOLD Science Data Products Guide and the GOLD Release Notes, both of which are available at: https://gold.cs.ucf.edu/data/documentation. The GOLD data product versions are provided at the website: https://gold.cs.ucf.edu/data/current-data-product-versions. The hourly resolution ap60 index data are obtained from GFZ Potsdam, Germany (Yamazaki, Matzka, Stolle, Kervalishvili, Rauberg, Bronkalla, & Jackson, 2022). Dst index data are from World Data Centre, Kyoto https://wdc.kugi.kyoto-u.ac.jp/. The solar F10.7 index data are from Space Weather Canada https://www.spaceweather.gc.ca/forecast-prevision/solar-solaire/solarflux/sx-en.php. The global 5-min cadence Total Electron Content (TEC) data are obtained from the Madrigal Database at Millstone Hill, http://millstonehill.haystack.mit.edu/.

Acknowledgments
We are indebted to the Science Data Center teams at LASP and the University of Central Florida. We thank Jürgen Matzka and Yosuke Yamazaki for alerting us to the availability of ap60 version 3.0 data used in this letter. In honor of Dr. Jennifer Gannon (CPI Vice President and co-worker of JSE, JC, and JDL), who passed away suddenly and tragically on May 2 at an early stage in her remarkable career, we propose to name the May 10–12 event the Gannon superstorm. We encourage members of the research community to join us in this way to honor Jenn's valuable contributions to the field of space weather. This work was supported by NASA Grant 80GSFC18C0061.

References

Aryal, S., Evans, J. S., Ajello, J., Solomon, S., Burns, A., Eastes, R., & McClintock, W. (2022). Constraining the upper level vibrational populations of the n2 lyman-birge-hopfield band system using gold mission's dayglow observations. *Journal of Geophysical Research: Space Physics*, *127*(9), e2021JA029869. https://doi.org/10.1029/2021ja029869

Babcock, J. R. R., & Evans, J. V. (1979). Effects of geomagnetic disturbances on neutral winds and temperatures in the thermosphere observed over Millstone Hill. *Journal of Geophysical Research*, *84*(A9), 5349–5354. https://doi.org/10.1029/JA084iA09p05349

Barth, C., Mankoff, K. D., Bailey, S., & Solomon, S. (2003). Global observations of nitric oxide in the thermosphere. *Journal of Geophysical Research*, *108*(A1). https://doi.org/10.1029/2002ja009458

Barth, C. A. (1992). Nitric oxide in the lower thermosphere. *Planetary and Space Science*, *40*(2–3), 315–336. https://doi.org/10.1016/0032-0633(92)90067-x

Budzien, S., Feldman, P., & Conway, R. (1994). Observations of the far ultraviolet airglow by the ultraviolet limb imaging experiment on sts-39. *Journal of Geophysical Research*, *99*(A12), 23275–23287. https://doi.org/10.1029/94ja01543

Buonsanto, M. J. (1999). Ionospheric storms — A review. *Space Science Reviews*, *88*(3/4), 563–601. https://doi.org/10.1023/A:1005107532631

Burns, A., Killeen, T., & Roble, R. (1989). Causes of changes in composition calculated using a thermospheric general circulation model. *Journal of Geophysical Research*, *94*(A4), 3670–3686. https://doi.org/10.1029/ja094ia04p03670

Burns, A. G., Killeen, T. L., Deng, W., Carignan, G. R., & Roble, R. G. (1995). Geomagnetic storm effects in the low-to middle-latitude upper thermosphere. *Journal of Geophysical Research*, *100*(A8), 14673–14692. https://doi.org/10.1029/94JA03232

Burns, A. G., Killeen, T. L., & Roble, R. G. (1991). A theoretical study of thermospheric composition perturbations during a impulsive geomagnetic storm. *Journal of Geophysical Research*, *96*(A8), 14153–14167. https://doi.org/10.1029/91JA00678

Cai, X., Burns, A. G., Wang, W., Qian, L., Solomon, S. C., Eastes, R. W., et al. (2020). The two-dimensional evolution of thermospheric $\sum O/N_2$ response to weak geomagnetic activity during solar-minimum observed by GOLD. *Geophysical Research Letters*, *47*(18), e88838. https://doi.org/10.1029/2020GL088838

Cai, X., Wang, W., Lin, D., Eastes, R. W., Qian, L., Zhu, Q., et al. (2023). Investigation of the southern hemisphere mid-high latitude thermospheric o/n2 responses to the space-x storm. *Journal of Geophysical Research: Space Physics*, *128*(3), e2022JA031002. https://doi.org/10.1029/2022ja031002

Codrescu, M., Fuller-Rowell, T., Roble, R., & Evans, D. (1997). Medium energy particle precipitation influences on the mesosphere and lower thermosphere. *Journal of Geophysical Research*, *102*(A9), 19977–19987. https://doi.org/10.1029/97ja01728

Collaboration, A., Price-Whelan, A. M., Lim, P. L., Earl, N., Starkman, N., Bradley, L., et al. (2022). The Astropy project: Sustaining and growing a community-oriented open-source project and the latest major Release (v5.0) of the core package. *The Astrophysical Journal*, *935*(2), 167. https://doi.org/10.3847/1538-4357/ac7c74

Correira, J., Evans, J. S., Lumpe, J., Krywonos, A., Daniell, R., Veibell, V., et al. (2021). Thermospheric composition and solar euv flux from the global-scale observations of the limb and disk (gold) mission. *Journal of Geophysical Research: Space Physics*, *126*(12), e2021JA029517. https://doi.org/10.1029/2021ja029517

Craven, J. D., Nicholas, A. C., Frank, L. A., Strickland, D. J., & Immel, T. J. (1994). Variations in the FUV dayglow after intense auroral activity. *Geophysical Research Letters*, *21*(25), 2793–2796. https://doi.org/10.1029/94GL02458

Crowley, G., Emery, B. A., Roble, R. G., Carlson, J. H. C., & Knipp, D. J. (1989a). Thermospheric dynamics during September 18-19, 1984 1. Model simulations. *Journal of Geophysical Research*, *94*(A12), 16925–16944. https://doi.org/10.1029/JA094iA12p16925

Crowley, G., Emery, B. A., Roble, R. G., Carlson, J. H. C., Salah, J. E., Wickwar, V. B., et al. (1989b). Thermospheric dynamics during September 18-19, 1984 2. Validation of the NCAR thermospheric general circulation model. *Journal of Geophysical Research*, *94*(A12), 16945–16959. https://doi.org/10.1029/JA094iA12p16945

Crowley, G., Schoendorf, J., Roble, R. G., & Marcos, F. A. (1995). Satellite observations of neutral density cells in the lower thermosphere at high latitudes. *Geophysical Monograph Series*, *87*, 339–348. https://doi.org/10.1029/GM087p0339

Eastes, R. W., McClintock, W. E., Burns, A. G., Anderson, D. N., Andersson, L., Codrescu, M., et al. (2017). The global-scale observations of the limb and disk (GOLD) mission. *Space Science Reviews*, *212*(1–2), 383–408. https://doi.org/10.1007/s11214-017-0392-2

Emery, B. A., Lathuillere, C., Richards, P. G., Roble, R. G., Buonsanto, M. J., Knipp, D. J., et al. (1999). Time dependent thermospheric neutral response tothe 2-11 November 1993 storm period. *Journal of Atmospheric and Solar-Terrestrial Physics*, *61*(3–4), 329–350. https://doi.org/10.1016/S1364-6826(98)00137-0

Emmert, J., Fejer, B. G., Shepherd, G., & Solheim, B. (2004). Average nighttime f region disturbance neutral winds measured by uars windii: Initial results. *Geophysical Research Letters*, *31*(22). https://doi.org/10.1029/2004gl021611

Evans, J., Eastes, R., Lumpe, J., Correira, J., Aryal, S., Laskar, F., et al. (2024). Disk images of neutral temperature from the global-scale observations of the limb and disk (gold) mission. *Journal of Geophysical Research: Space Physics*, *129*(6). https://doi.org/10.1029/2024JA032424

Evans, J., Strickland, D., & Huffman, R. (1995). Satellite remote sensing of thermospheric O/N_2 and solar EUV. 2: Data analysis. *Journal of Geophysical Research*, *100*(A7), 12227–12233. https://doi.org/10.1029/95JA00573

Evans, J. V., Holt, J. M., & Wand, R. H. (1979). Millstone Hill incoherent scatter observations of auroral convection over 60°?Λ?75° 1, Observing and data reduction procedures. *Journal of Geophysical Research*, *84*(A12), 7059–7074. https://doi.org/10.1029/JA084iA12p07059

Fuller-Rowell, T. J., Codrescu, M. V., Fejer, B. G., Borer, W., Marcos, F., & Anderson, D. N. (1997). Dynamics of the low-latitude thermosphere: Quiet and disturbed conditions. *Journal of Atmospheric and Solar-Terrestrial Physics*, *59*(13), 1533–1540. https://doi.org/10.1016/S1364-6826(96)00154-X

Fuller-Rowell, T. J., Codrescu, M. V., Risbeth, H., Moffett, R. J., & Quegan, S. (1996). On the seasonal response of the thermosphere and ionosphere to geomagnetic storms. *Journal of Geophysical Research*, *101*(A2), 2343–2354. https://doi.org/10.1029/95JA01614

Fuller-Rowell, T. J., Millward, G. H., Richmond, A. D., & Codrescu, M. V. (2002). Storm-time changes in the upper atmosphere at low latitudes. *Journal of Atmospheric and Solar-Terrestrial Physics*, *64*(12–14), 1383–1391. https://doi.org/10.1016/S1364-6826(02)00101-3

Galand, M., Roble, R., & Lummerzheim, D. (1999). Ionization by energetic protons in thermosphere-ionosphere electrodynamics general circulation model. *Journal of Geophysical Research*, *104*(A12), 27973–27989. https://doi.org/10.1029/1999ja900374

Gan, Q., Eastes, R. W., Burns, A. G., Wang, W., Qian, L., Solomon, S. C., et al. (2020). First synoptic observations of geomagnetic storm effects on the global-scale OI 135.6-nm dayglow in the thermosphere by the GOLD mission. *Geophysical Research Letters*, *47*(3), e85400. https://doi.org/10.1029/2019GL085400

Gan, Q., Eastes, R. W., Wu, Y.-J., Qian, L., Cai, X., Wang, W., et al. (2024). Thermospheric responses to the 3 and 4 november 2021 geomagnetic storm during the main and recovery phases as observed by NASA's GOLD and ICON missions. *Geophysical Research Letters*, *51*(4), e2023GL106529. https://doi.org/10.1029/2023GL106529

Gardner, L. C., & Schunk, R. W. (2010). Generation of traveling atmospheric disturbances during pulsating geomagnetic storms. *Journal of Geophysical Research (Space Physics)*, *115*(A8), A08314. https://doi.org/10.1029/2009JA015129

Gérard, J.-C., & Barth, C. (1977). High-latitude nitric oxide in the lower thermosphere. *Journal of Geophysical Research*, *82*(4), 674–680. https://doi.org/10.1029/ja082i004p00674

Hayakawa, H., Ebihara, Y., & Pevtsov, A. A. (2024). Analyses of equatorward auroral extensions during the extreme geomagnetic storm on 15 July 1959. *Monthly Notices of the Royal Astronomical Society*, *527*(3), 7298–7305. https://doi.org/10.1093/mnras/stad3556

Laskar, F. I., Eastes, R. W., Codrescu, M. V., Evans, J. S., Burns, A. G., Wang, W., et al. (2021). Response of gold retrieved thermospheric temperatures to geomagnetic activities of varying magnitudes. *Geophysical Research Letters*, *48*(15), e2021GL093905. https://doi.org/10.1029/2021gl093905

Laskar, F. I., Pedatella, N. M., Codrescu, M. V., Eastes, R. W., & McClintock, W. E. (2022). Improving the thermosphere ionosphere in a whole atmosphere model by assimilating gold disk temperatures. *Journal of Geophysical Research: Space Physics*, *127*(3), e2021JA030045. https://doi.org/10.1029/2021ja030045

Li, J., Wang, W., Lu, J., Yue, J., Burns, A. G., Yuan, T., et al. (2019). A modeling study of the responses of mesosphere and lower thermosphere winds to geomagnetic storms at middle latitudes. *Journal of Geophysical Research (Space Physics)*, *124*(5), 3666–3680. https://doi.org/10.1029/2019JA026533

McClintock, W. E., Eastes, R. W., Beland, S., Bryant, K. B., Burns, A. G., Correira, J., et al. (2020). Global-scale observations of the limb and disk mission implementation: 2. Observations, data pipeline, and level 1 data products. *Journal of Geophysical Research: Space Physics*, *125*(5), e2020JA027809. https://doi.org/10.1029/2020ja027809

Meier, R. R., Crowley, G., Strickland, D. J., Christensen, A. B., Paxton, L. J., Morrison, D., & Hackert, C. L. (2005). First look at the 20 November 2003 superstorm with TIMED/GUVI: Comparisons with a thermospheric global circulation model. *Journal of Geophysical Research (Space Physics)*, *110*(A9), 9. https://doi.org/10.1029/2004JA010990

Meriwether, J. W. (2008). Thermospheric dynamics at low and mid-latitudes during magnetic storm activity. *Geophysical Monograph Series*, *181*, 201–219. https://doi.org/10.1029/181GM19

Mlynczak, M., Martin-Torres, F. J., Russell, J., Beaumont, K., Jacobson, S., Kozyra, J., et al. (2003). The natural thermostat of nitric oxide emission at 5.3 μm in the thermosphere observed during the solar storms of april 2002. *Geophysical Research Letters*, *30*(21). https://doi.org/10.1029/2003gl017693

O'Callaghan, J., & Billings, L. (2024). The strongest solar storm in 20 years did little damage, but worse space weather is coming. *Scientific American*. Retrieved from https://www.scientificamerican.com/article/the-strongest-solar-storm-in-20-years-did-little-damage-but-worse-space/

Proelss, G. W. (1980). Magnetic storm associated perturbations of the upper atmosphere - recent results obtained by satellite-borne gas analyzers. *Reviews of Geophysics and Space Physics*, *18*(1), 183–202. https://doi.org/10.1029/RG018i001p00183

Proelss, G. W. (1987). Storm-induced changes in the thermospheric composition at middle latitudes. *Planetary and Space Science*, *35*(6), 807–811. https://doi.org/10.1016/0032-0633(87)90041-9

Richmond, A. D., & Lu, G. (2000). Upper-atmospheric effects of magnetic storms: A brief tutorial. *Journal of Atmospheric and Solar-Terrestrial Physics*, *62*(12), 1115–1127. https://doi.org/10.1016/S1364-6826(00)00094-8

Rishbeth, H. (1989). F-region storms and thermospheric circulation. In *Electromagnetic coupling in the polar clefts and caps* (pp. 393–406). Springer.

Roble, R. (1992). The polar lower thermosphere. *Planetary and Space Science*, *40*(2–3), 271–297. https://doi.org/10.1016/0032-0633(92)90065-v

Straus, J. M., & Schulz, M. (1976). Magnetospheric convection and upper atmospheric dynamics. *Journal of Geophysical Research*, *81*(A34), 5822–5832. https://doi.org/10.1029/JA081i034p05822

Strickland, D. J., Daniell, R. E., & Craven, J. D. (2001). Negative ionospheric storm coincident with DE 1-observed thermospheric disturbance on October 14, 1981. *Journal of Geophysical Research*, *106*(A10), 21049–21062. https://doi.org/10.1029/2000JA000209

Strickland, D. J., Evans, J. S., & Paxton, L. J. (1995). Satellite remote sensing of thermospheric O/N_2 and solar EUV. 1: Theory. *Journal of Geophysical Research*, *100*(A7), 12217–12226. https://doi.org/10.1029/95JA00574

Yamazaki, Y., Matzka, J., Stolle, C., Kervalishvili, G., Rauberg, J., Bronkalla, O., et al. (2022). Geomagnetic hpo index v. 3.0 [Dataset]. https://kp.gfz-potsdam.de/en/hp30-hp60

Yamazaki, Y., Matzka, J., Stolle, C., Kervalishvili, G., Rauberg, J., Bronkalla, O., et al. (2022). Geomagnetic activity index hpo. *Geophysical Research Letters*, *49*(10). https://doi.org/10.1029/2022gl098860

Yu, T., Wang, W., Ren, Z., Cai, X., Yue, X., & He, M. (2021). The response of middle thermosphere (160 km) composition to the November 20 and 21, 2003 superstorm. *Journal of Geophysical Research: Space Physics*, *126*(10), e2021JA029449. https://doi.org/10.1029/2021ja029449

Zhang, Y., Paxton, L. J., Morrison, D., Marsh, D., & Kil, H. (2014). Storm-time behaviors of O/N_2 and NO variations. *Journal of Atmospheric and Solar-Terrestrial Physics*, *114*, 42–49. https://doi.org/10.1016/j.jastp.2014.04.003